Regime transition in the energy cascade of rotating turbulence

T. Pestana* and S. Hickel
Aerodynamics Group, Faculty of Aerospace Engineering, Delft University of Technology, Kluyverweg 2, 2629 HS Delft, The Netherlands

(Received 2 November 2018; revised manuscript received 14 February 2019; published 8 May 2019)

Transition from a split to a forward kinetic energy cascade system is explored in the context of rotating turbulence using direct numerical simulations with a three-dimensional isotropic random force uncorrelated with the velocity field. Our parametric study covers confinement effects in high-aspect-ratio domains and a broad range of rotation rates. The data presented here add substantially to previous works, which, in contrast, focused on smaller and shallower domains. Results indicate that for fixed geometrical dimensions the Rossby number acts as a control parameter, whereas for a fixed Rossby number the product of the domain size along the rotation axis and the forcing wave number governs the amount of energy that cascades inversely. The regime transition criterion hence depends on both control parameters.

DOI: 10.1103/PhysRevE.99.053103

I. INTRODUCTION

The energy cascade is the fundamental mechanism in turbulent flows that describes the energy exchange between the various scales of motion [1]. A forward cascade from large to small scales is commonly observed in three-dimensional (3D) flows, whereas an inverse energy cascade from small towards large scales is the hallmark of two-dimensional (2D) flows [2,3]. Predicting the energy cascade direction, therefore, requires anticipating if, for a given set of control parameters, the resulting flow field resembles best 3D or 2D flow dynamics. In the absence of analytical predictions, a typical approach consists of carefully designing numerical experiments, where the system's parameters are individually varied to produce a phase transition diagram. Throughout this study we consider a large number of forced direct numerical simulations (DNSs) and analyze the influence of geometric confinement and system rotation on the cascade direction in homogeneous rotating turbulence.

Inertial waves, i.e., plane-wave solutions to the linearized Navier-Stokes equations, can modulate the energy transfer in rotating turbulence [4,5]. By considering high rotation rates and exploiting the fact that rotating turbulence is a multi-time-scale problem, Waleffe [6] suggested that the nonlinear dynamics are modified by wave interactions. Resonant wave interactions can explain the favored energy transfer towards horizontal modes, whereas nonresonant wave interactions are considered to damp and inhibit the triadic interactions typical of homogeneous turbulence [7,8]. This mechanism also persists at lower rotation rates due to homochirical interactions that transfer energy into the plane orthogonal to the rotation axis [9]. As a consequence, when rotating homogeneous flows are forced at wave number κ_f, the injected energy can cascade both to larger ($\kappa < \kappa_f$) and to smaller scales ($\kappa > \kappa_f$); this is hereafter referred to as a split energy cascade. These findings help to explain the preferential upscale of energy typically found in numerical and experimental investigations of rotating turbulent flows [8,10–14]. Nevertheless, we must bear in mind that a large network of triadic interactions as in the Navier-Stokes equations can evolve differently than a set of isolated triads, as previously pointed out in Refs. [15] and [16].

Among different theories that elucidate the phenomenon of rotating turbulence, the work of Galtier [17] is regarded as an important contribution. Based on wave turbulence theory, which deals with systems where interactions are governed by waves, he derived scaling laws for the energy spectrum. These laws were also shown to follow from phenomenological arguments for the spectral transfer time—a typical energy transfer time scale. For infinitely large domains, as required by wave turbulence theory [18], the weak inertial-wave theory of Galtier [17] predicts that energy cascades forward and to small scales. However, a passage from a split to a forward energy cascade system upon approaching the large-box limit has not yet been confirmed by DNS.

In the absence of rotation, however, the geometrical dimensions of the system itself influence the energy cascade direction. Using a two-dimensional, two-component (2D2C) horizontal force, Smith *et al.* [19] and Celani *et al.* [20] found that the ratio L_3/ℓ_f, where L_3 is the vertical domain extension and ℓ_f is the forcing length scale, is a governing control parameter. They showed that a large L_3/ℓ_f results in a forward energy cascade, whereas an inverse energy transfer was triggered and split the energy cascade for $L_3/\ell_f \leqslant 1/2$. More recently, numerical simulations by Benavides and Alexakis [21] explored transitions in a thin layer of fluid subjected to free-slip boundary conditions. Transition from a forward to a split energy cascade was shown to be critical and depend on the ratio of forcing length scale to wall separation.

Regime transitions in rotating homogeneous turbulence are therefore affected by geometrical dimensions and rotation rate. Deusebio *et al.* [22] studied hyperviscous fluids in rotating low-aspect-ratio domains subjected to 2D2C forcing and found that high rotation rates as well as small L_3/ℓ_f suppress enstrophy production and induce an inverse energy cascade. Their data prove, at least for weak rotation rates, that transition

*t.pestana@tudelft.nl

from a split to a forward cascade is possible by controlling either the rotation rate or the domain size. For strong rotation, however, almost the entire injected energy cascaded inversely. Although transition was not observed, they hypothesized that it could still take place for sufficiently large L_3/ℓ_f. This conjecture, however, remains to be verified by either forcing smaller flow scales or increasing the domain size [23].

The present work sheds light on the question whether a transition from a split to a forward cascade system always exists in forced homogeneous rotating turbulence. We conduct a systematic parametric study that covers several rotation rates and an unprecedented range of geometric confinements by considering strongly elongated domains and large forcing wave numbers κ_f. This new database is complementary to previous studies, which focused on the confinement-induced transition in smaller and shallower domains. Through large-scale forcing, we construct isotropic flow fields that are posteriorly subjected to rotation. Differently from previous studies, we employ a three-dimensional, three-component (3D3C) forcing scheme that by design provides a constant energy input independent of the velocity field. We believe this results in a neater and more general framework where anisotropy originates solely from rotation.

II. METHODOLOGY AND GOVERNING PARAMETERS

We solve the incompressible Navier-Stokes equations in a frame rotating at rate $\mathbf{\Omega}$:

$$\nabla \cdot \mathbf{u} = 0, \tag{1}$$

$$\frac{\partial \mathbf{u}}{\partial t} + (2\,\mathbf{\Omega} + \boldsymbol{\omega}) \times \mathbf{u} = -\nabla q + \nu \nabla^2 \mathbf{u} + \mathbf{f}. \tag{2}$$

Here, $\mathbf{u}$, $\boldsymbol{\omega}$, and $\mathbf{f}$ are the velocity, the vorticity, and an external force, respectively. The reduced pressure into which the centrifugal force is incorporated is given by q, and ν denotes the kinematic viscosity.

Equations (1) and (2) are discretized in space by a dealiased Fourier pseudospectral method (2/3 rule) in a triply periodic domain of size $2\pi\mathcal{L}_1 \times 2\pi\mathcal{L}_2 \times 2\pi\mathcal{L}_3$ [24,25]. The rotation axis is assumed to be aligned with the vertical direction, i.e., $\mathbf{\Omega} = \Omega\,\hat{\mathbf{e}}_3$, and we restrict ourselves to cases where the domain sizes in the directions perpendicular to the axis of rotation are equal: $\mathcal{L}_1 = \mathcal{L}_2 = \mathcal{L}_\perp = 1$. Accordingly, $\mathcal{L}_\parallel$ replaces $\mathcal{L}_3$ to denote the domain size in the direction parallel to the rotation axis and can be arbitrarily chosen. We use Rogallo's integrating factor technique for exact time integration of the viscous and Coriolis terms and a third-order Runge-Kutta scheme for the nonlinear terms [26,27].

The external force $\mathbf{f}$ injects energy to the system at rate ε_I; see Ref. [28]. The force's spectrum $F(\kappa)$, from which $\mathbf{f}$ in Eq. (2) is assembled, is Gaussian distributed, centered around a wave number κ_f, and has standard deviation $c = 0.5$: $F(\kappa) = A\exp(-(\kappa - \kappa_f)^2/c)$. For a given κ_f and c, the prefactor A is uniquely determined from the desired energy input rate ε_I. In the absence of rotation, we obtain isotropic velocity fields and a balance between the energy input rate and the viscous dissipation, i.e., $\varepsilon_I = \varepsilon_\nu$. This forcing scheme ensures through projection that the force and velocity field are uncorrelated at every instant in time [28]. As a consequence, ε_I is solely determined by the force-force correlation and is independent of the velocity field. Thus, we can define *a priori* true control parameters from which the governing nondimensional numbers are derived.

The domain size, $\mathcal{L}_\parallel$ and $\mathcal{L}_\perp$, the forcing wave number κ_f, the viscosity ν, the rotation rate Ω, and the energy input rate ε_I can all be freely chosen. Regarding ε_I, it could be additionally decomposed into three contributions stemming from the power injected in each direction. However, because the forcing is isotropic, it is sufficient to consider the total power input ε_I only. These six parameters $\{\kappa_f, \nu, \varepsilon_I, \Omega, \mathcal{L}_\perp, \mathcal{L}_\parallel\}$ form the set of true control parameters and are the basis for the nondimensional similarity numbers. The characteristic length, velocity and time-scale follow naturally as $\ell_f = \kappa_f^{-1}$, $u_f = \varepsilon_I^{1/3}\,\kappa_f^{-1/3}$, and $\tau_f = \kappa_f^{-2/3}\,\varepsilon_I^{-1/3}$, respectively. In addition, a time scale based on the rotation rate is taken as $\tau_\Omega = 1/(2\Omega)$.

The Reynolds and Rossby numbers are now unambiguously defined as

$$\mathrm{Re}_\varepsilon = \frac{\varepsilon_I^{1/3}\,\kappa_f^{-4/3}}{\nu} \quad \text{and} \quad \mathrm{Ro}_\varepsilon = \frac{\kappa_f^{2/3}\varepsilon_I^{1/3}}{2\Omega}. \tag{3}$$

From the problem's geometry and the forcing wave number, we define two other nondimensional numbers, i.e., $\kappa_f\mathcal{L}_\perp$ and $\kappa_f\mathcal{L}_\parallel$. Hence, we obtain a set of four independent governing nondimensional numbers that fully describes our numerical experiments: Re_ε, Ro_ε, $\kappa_f\mathcal{L}_\perp$, and $\kappa_f\mathcal{L}_\parallel$. As the final goal is to investigate dimensional and rotational effects on forced homogeneous rotating turbulence, we fix Re_ε and allow Ro_ε, $\kappa_f\mathcal{L}_\parallel$, and $\kappa_f\mathcal{L}_\perp$ to vary. We remark that this set is not unique and other nondimensional groups exist. For instance, Re_ε and Ro_λ could be combined to form the microscale Rossby number $\mathrm{Ro}_\lambda = {\mathrm{Re}_\varepsilon}^{1/2}\mathrm{Ro}_\lambda$ (ratio of rotation and Kolmogorov

TABLE I. List of direct numerical simulations at $\mathrm{Re}_\varepsilon \approx 55$. Ro_ε numbers are given in the footnotes.

Case	$\kappa_f\mathcal{L}_\perp$	$\kappa_f\mathcal{L}_\parallel$	A_r	N_p
kf02-a01[a]	2	2	1	192^3
kf04-a01[a]	4	4	1	384^3
kf04-a02[b]	4	8	2	$384^2 \times 768$
kf04-a04[b]	4	16	4	$384^2 \times 1536$
kf04-a08[b]	4	32	8	$384^2 \times 3072$
kf04-a16[b]	4	64	16	$384^2 \times 6144$
kf04-a32[b]	4	128	32	$384^2 \times 12288$
kf08-a01[a]	8	8	1	768^3
kf08-a02[b]	8	16	2	$768^2 \times 1536$
kf08-a04[b]	8	32	4	$768^2 \times 3072$
kf08-a08[c]	8	64	8	$768^2 \times 6144$
kf08-a16[b]	8	128	16	$768^2 \times 12288$
kf16-a01[a]	16	16	1	1536^3
kf16-a02[b]	16	32	2	$1536^2 \times 3072$
kf16-a04[b]	16	64	4	$1536^2 \times 6144$
kf32-a01[b]	32	32	1	3072^3

[a] $\mathrm{Ro}_\varepsilon \approx 0.31, 0.06$.
[b] $\mathrm{Ro}_\varepsilon \approx 0.06$.
[c] $\mathrm{Ro}_\varepsilon \approx 1.25, 0.63, 0.31, 0.27, 0.24, 0.22, 0.19, 0.16, 0.14, 0.11, 0.09, 0.08, 0.06$.

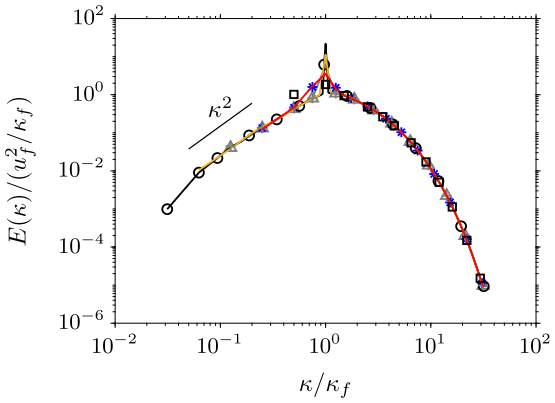

FIG. 1. Three-dimensional spherically averaged energy spectrum of the initial condition: `kf02-a01` (□), `kf04-a01` (—), `kf08-a01` (+), `kf16-a01` (—), `kf32-a01` (—○—), `kf04-a32` (∗) `kf08-a16` (△).

time scale [7]) or $\kappa_f\mathcal{L}_\parallel$ and $\kappa_f\mathcal{L}_\perp$ could be related to obtain the domain's aspect ratio $A_r = \mathcal{L}_\parallel/\mathcal{L}_\perp$.

Initial conditions were generated by performing DNS of nonrotating forced isotropic turbulence. We started from a zero-velocity field and marched in time until a fully developed steady state was achieved. After the initial transient, statistics were sampled over at least $24\,\tau_f$, corresponding to approximately 10 large-eddy turnover times. Following this procedure, a reference isotropic solution was computed for every entry in Table I.

The initially imposed $\mathrm{Re}_\varepsilon \approx 55$ ultimately led to homogeneous nonrotating turbulent fields with a characteristic Taylor microscale Reynolds number $\mathrm{Re}_\lambda \approx 68$. The spatial resolution in terms of the Kolmogorov length scale η was kept constant throughout this study, i.e., $\kappa_{\max}\eta \approx 1.5$, where $\kappa_{\max}$ is the largest represented wave number. For the case with the largest $\kappa_f\mathcal{L}_\parallel$, the integral length scale in the direction of rotation is about 600 times smaller than the respective domain size.

Figure 1 compares the 3D spherically averaged energy spectrum $E(\kappa)$ for cases with aspect ratio $A_r = 1$, which contain "a01" in its name description, and two additional simulations with $A_r = 16$ and $A_r = 32$ (cases `kf04-a32` and `kf08-a16` in Table I). These data prove the equivalence between initial conditions for DNSs forced at different wave numbers and those computed with distinct $\kappa_f\mathcal{L}_\parallel$ and $\kappa_f\mathcal{L}_\perp$. We find that the energy spectra perfectly coincide and that $E(\kappa)$ scales best with κ^2 at wave numbers $\kappa < \kappa_f$, in agreement with Ref. [29]. The obtained isotropic velocity fields were used as the initial condition for simulations with different rotation rates. The statistical variability of the results for small domains was reduced by ensemble averaging. For the smallest domain, `kf02-a01`, we ensemble-averaged 10 independent realizations and cases `kf04` with $A_r > 1$ are averages of 3 realizations. For all other cases, the data correspond to a single numerical experiment.

III. RESULTS

First we assess the effects of geometrical dimension and rotation on the time evolution of the box-averaged kinetic energy K and viscous dissipation ε_ν. The nondimensional geometric parameters $\kappa_f\mathcal{L}_\perp$ and $\kappa_f\mathcal{L}_\parallel$ are varied for two fixed rotation rates: weak ($\mathrm{Ro}_\varepsilon = 0.31$; Fig. 2) and strong ($\mathrm{Ro}_\varepsilon = 0.06$; Fig. 3). Additionally, for a fixed and large domain, $\kappa_f\mathcal{L}_\perp = 8$ and $\kappa_f\mathcal{L}_\parallel = 64$ (case `kf08-a08`; Fig. 4), we investigate the Rossby number range $0.06 < \mathrm{Ro}_\varepsilon < 1.25$. For more details about the simulation parameters, please refer to Table I.

All cases undergo a transient of roughly $10\,\tau_f$ from the onset of rotation (Figs. 2 to 4), which converges towards a unique solution for sufficiently large $\kappa_f\mathcal{L}_\parallel$. We find that the results are independent of the transversal domain size for $\kappa_f\mathcal{L}_\perp \geqslant 4$; see Fig. 3, where the lines for different $\kappa_f\mathcal{L}_\perp$ and identical $\kappa_f\mathcal{L}_\parallel$ coincide. Departing from an isotropic state, where the energy cascade is strictly forward ($\varepsilon_\nu/\varepsilon_I = 1$), ε_ν decreases monotonically until it is lowest at approximately $3\,\tau_f$ [Figs. 2(b), 3(b) and 4(b)]. For fixed Ro_ε, Figs. 2(b) and 3(b) show that both $\kappa_f\mathcal{L}_\perp$ and $\kappa_f\mathcal{L}_\parallel$ have no influence on the minimum of ε_ν. On the other hand, Fig. 4(b) suggests a direct proportionality between the minimum value of ε_ν and Ro_ε.

After $t \approx 3\,\tau_f$, ε_ν increases towards ε_I. Nevertheless, the strong and weak rotation cases lead to a different final state for ε_ν. While increasing $\kappa_f\mathcal{L}_\parallel$ restores $\varepsilon_\nu = \varepsilon_I$ for the weak rotating case [Fig. 2(b)], the imbalance $\varepsilon_\nu < \varepsilon_I$, although lower than $0.075\,\varepsilon_I$ for $\kappa_f\mathcal{L}_\parallel = 128$, persists up to the final time for the strong rotating case [Fig. 3(b)]. Similarly to Fig. 2(b), increasing Ro_ε reestablishes a forward energy cascade for a fixed domain size [Fig. 4(b)]. After the initial transient ($t > 10\,\tau_f$), ε_ν follows mostly a slow linear decay [Fig. 3(b)] or remains nearly constant [Figs. 2(b) and 4(b)]. Consequently, K, which evolves in time as $dK/dt = \varepsilon_I - \varepsilon_\nu$, grows quasilinearly [Figs. 2(a), 3(a) and 4(a)]. Based on this idea we define the inverse energy flux $\varepsilon_{\mathrm{inv}} = \varepsilon_I - \varepsilon_\nu$ from the imbalance between energy injection rate and viscous dissipation. To estimate $\varepsilon_{\mathrm{inv}}$, which is equal to the local slope of $K(t)$, a linear least-squares fit is applied to $15\,\tau_f < t < 30\,\tau_f$ in the time evolution of K [Figs. 2(a), 3(a) and 4(a)]. The r.m.s. residual between the actual and the fitted data indicates that the linear regression model is appropriate. For the worst case, `kf04-a08`, the r.m.s. residual is 0.65% of the mean value. Assuming that the linear law is exact and the noise is essentially Gaussian, one obtains 0.0004 for the standard error of the slope coefficient. Results for the inverse energy flux are thus shown in Figs. 5 and 6 in the form of a phase transition diagram.

In Fig. 5(a), we see that the inverse energy flux $\varepsilon_{\mathrm{inv}}$ decreases monotonically with $\kappa_f\mathcal{L}_\parallel$ for both $\mathrm{Ro}_\varepsilon \approx 0.31$ and $\mathrm{Ro}_\varepsilon \approx 0.06$. Moreover, results for the strong rotating case suggest that increasing $\kappa_f\mathcal{L}_\perp$ while retaining $\kappa_f\mathcal{L}_\parallel$ leads to negligible differences in $\varepsilon_{\mathrm{inv}}$; see the overlapping circles of different colors for $\mathrm{Ro}_\varepsilon \approx 0.06$. Transition from a split to a forward cascade system occurs gradually. For $\mathrm{Ro}_\varepsilon \approx 0.31$ and $\kappa_f\mathcal{L}_\parallel = 64$ less than $0.004\varepsilon_I$ is transferred in the inverse direction, whereas for $\mathrm{Ro}_\varepsilon \approx 0.06$ a split cascade is still present at $\kappa_f\mathcal{L}_\parallel = 128$. For a fixed domain size with $\kappa_f\mathcal{L}_\perp = 8$ and $\kappa_f\mathcal{L}_\parallel = 64$ [case `kf08-a08`; Fig. 5(b)], $\varepsilon_{\mathrm{inv}}$ is continuously suppressed for increasing Ro_ε and transition to a forward cascade system occurs in the vicinity of $\mathrm{Ro}_\varepsilon = 1$.

A question that follows from these results is for which combination of governing nondimensional parameters regime transition occurs. From the literature, a possible criterion is

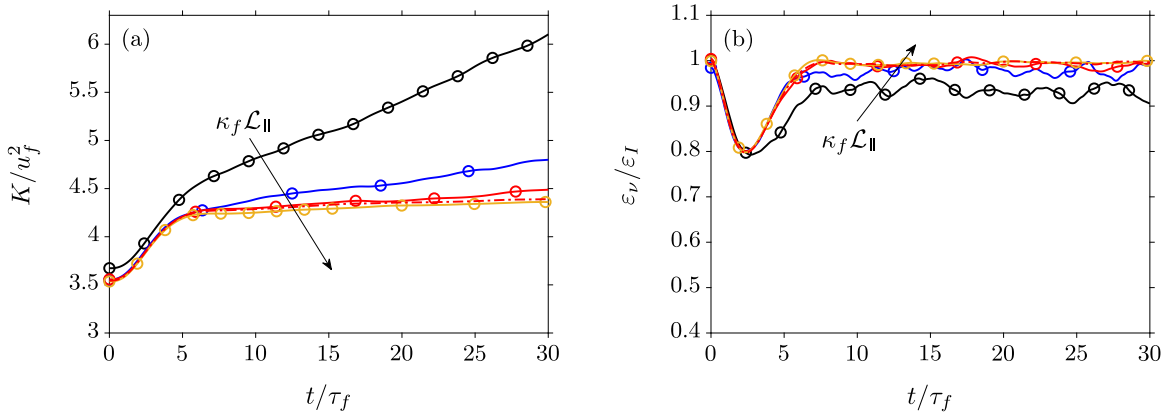

FIG. 2. Time evolution of box-averaged kinetic energy (a) and energy dissipation rate (b) for $\mathrm{Ro}_\varepsilon \approx 0.31$ (weak rotation). Lines corresponding to the same $\kappa_f\mathcal{L}_\perp$ are grouped by color: $\kappa_f\mathcal{L}_\perp = 2$ (■), $\kappa_f\mathcal{L}_\perp = 4$ (■), $\kappa_f\mathcal{L}_\perp = 8$ (■), and $\kappa_f\mathcal{L}_\perp = 16$ (■). Lines corresponding to the same A_r are grouped by type: $A_r = 1$ (—○—), $A_r = 8$ (_ _ _) (cf. Table I).

$\mathrm{Ro}_\varepsilon\kappa_f\mathcal{L}_\parallel = C$, where C is a constant [2,23]. To test this hypothesis, Fig. 6 presents the data from Fig. 5, but juxtaposed in a single diagram and scaled accordingly with $\mathrm{Ro}_\varepsilon\kappa_f\mathcal{L}_\parallel$. The curves for different Ro_ε values do not line up; hence, this criterion disagrees with our data. Discussion of a possible reason is given in the next section.

Now we turn our attention to the influence of $\kappa_f\mathcal{L}_\parallel$ and $\kappa_f\mathcal{L}_\perp$ on the spectral energy flux and energy spectra. Hereafter we present results for the strong rotating case with $\mathrm{Ro}_\varepsilon \approx 0.06$ only, as differences are more pronounced than in the weak rotating case. Although we show instantaneous data at $t = 30\,\tau_f$, the trend described in what follows also holds for other instants in time. Conservation of energy requires the portion of the injected energy that is not dissipated to be accumulated. By analyzing the spectral energy flux $\Pi(\kappa)$, we find that the net energy transfer $T(\kappa) = -d\Pi/d\kappa$ is positive for $\kappa < \kappa_f$. In other words, wave numbers in this range gain energy and we observe an upscale energy transfer. Evidence is presented in Fig. 7, which also highlights how sensitive $\Pi(\kappa)$ is with respect to changes in $\kappa_f\mathcal{L}_\parallel$ and $\kappa_f\mathcal{L}_\perp$. In this regard, Fig. 7(a), where $\kappa_f\mathcal{L}_\parallel$ is constant and $\kappa_f\mathcal{L}_\perp = \{8, 16, 32\}$, shows that the shape of $\Pi(\kappa)$ remains unaltered for different $\kappa_f\mathcal{L}_\perp$ values. On the other hand, varying $\kappa_f\mathcal{L}_\parallel$ from 16 to 64, while $\kappa_f\mathcal{L}_\perp$ is constant, reduces the magnitude of the inverse energy flux and the range of wave numbers for which an upscale energy transfer takes place [see Fig. 7(b)]. Therein, greater values of $\kappa_f\mathcal{L}_\parallel$ are also associated with an enhanced spectral energy flux for $\kappa > \kappa_f$. This is a consequence of the fixed energy input rate ε_I, which causes the step in $\Pi(\kappa)$ at $\kappa = \kappa_f$ to be the same in all cases.

The 3D energy spectra $E(\kappa)$ for the same cases are shown in Fig. 8. Additionally, the energy spectrum of case `kf32-a01` with $\kappa_f\mathcal{L}_\parallel = \kappa_f\mathcal{L}_\perp = 32$ from Fig. 1 at the onset of rotation is included as a reference. Figure 8(a) reinforces that $\kappa_f\mathcal{L}_\parallel$ dictates the degree of energy accumulation, as the curves for different $\kappa_f\mathcal{L}_\perp$ and constant $\kappa_f\mathcal{L}_\parallel$ values overlap. In agreement with results in Fig. 7 for $\Pi(\kappa)$, we observe significantly higher levels of energy for $\kappa < \kappa_f$ with respect to the isotropic reference spectrum. These are reduced for increasing $\kappa_f\mathcal{L}_\parallel$ [see Fig. 8(b)].

As for the distribution of energy in terms of $\kappa_\parallel$ and $\kappa_\perp$, Fig. 9 presents the 2D energy spectrum $E(\kappa_\perp, \kappa_\parallel)$. Results

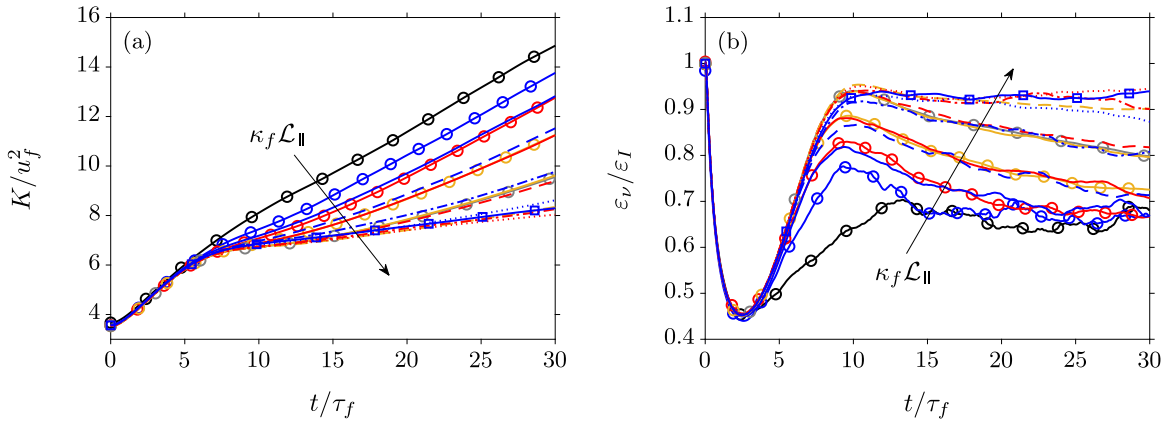

FIG. 3. Time evolution of box-averaged kinetic energy (a) and energy dissipation rate (b) for $\mathrm{Ro}_\varepsilon \approx 0.06$ (strong rotation). Lines corresponding to the same $\kappa_f\mathcal{L}_\perp$ are grouped by color: $\kappa_f\mathcal{L}_\perp = 2$ (■), $\kappa_f\mathcal{L}_\perp = 4$ (■), $\kappa_f\mathcal{L}_\perp = 8$ (■), $\kappa_f\mathcal{L}_\perp = 16$ (■), $\kappa_f\mathcal{L}_\perp = 32$ (■). Lines corresponding to the same A_r are grouped by type: $A_r = 1$ (—○—), $A_r = 2$ (_), $A_r = 4$ (_ _), $A_r = 8$ (_ _ _), $A_r = 16$ (.....), $A_r = 32$ (—□—) (cf. Table I).

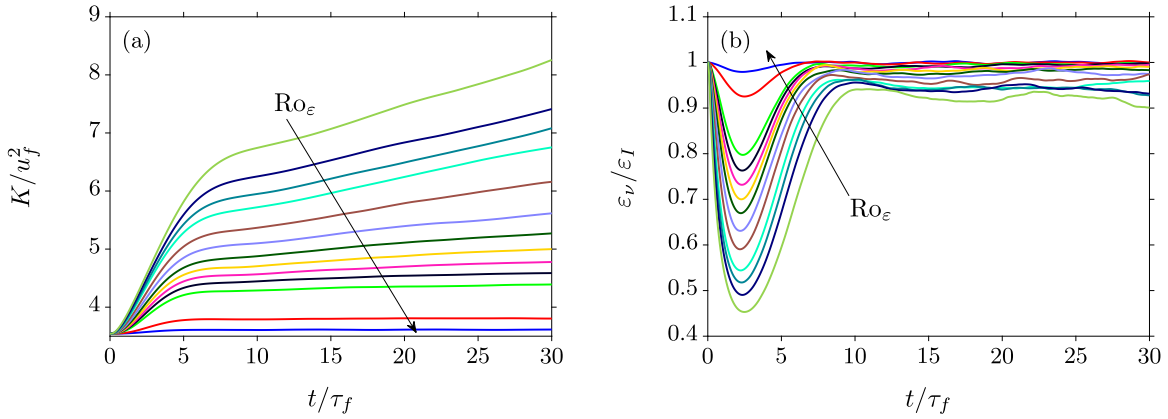

FIG. 4. Time evolution of box-averaged kinetic energy (a) and energy dissipation rate (b) for $\kappa_f\mathcal{L}_\perp = 8$ and $\kappa_f\mathcal{L}_\parallel = 64$. Different line colors correspond to the range $0.06 < \mathrm{Ro}_\varepsilon < 1.25$; see Table I.

are shown exclusively for case `kf32-a01` with $\kappa_f\mathcal{L}_\perp = \kappa_f\mathcal{L}_\parallel = 32$, as it provides the best large-scale resolution. The energy spectrum is nondimensionalized with $2\pi\kappa_\perp$, in such a way that contour levels of isotropic spectra appear as circles centered at the origin. In agreement with previous works, Fig. 9 confirms that the kinetic energy has the tendency to accumulate at lower $\kappa_\parallel/\kappa_f$. Hence, $E(\kappa_\perp, \kappa_\parallel)$ is anisotropic and contour levels display an elliptical shape, with the major axis aligned with the $\kappa_\perp$ direction. This is observed even for high wave numbers and suggests that all scales of motion are influenced by rotation; indeed, for this case, $\kappa_\Omega\eta = 1.1$, where $\kappa_\Omega = (\Omega^3/\varepsilon_I)^{1/2}$ is the Zeman wave number [14]. At the same time, the energy input remains isotropic. See the inset for the imprint of the isotropic forcing scheme, which delineates the bright area located at $\kappa_\parallel^2 + \kappa_\perp^2 = \kappa_f^2$. In addition, we see higher energy levels in the vicinity of $\kappa_\parallel/\kappa_f = 0$.

An anisotropic distribution of energy is predicted by the weak inertial-wave theory, which suggests that the energy spectrum has the form $E(\kappa_\perp, \kappa_\parallel) \sim \kappa_\perp^{-5/2}\kappa_\parallel^{-1/2}$ [17]. To test whether our data present any sign of this scaling law, we show in Fig. 10 instantaneous one-dimensional energy spectra along the perpendicular and parallel directions, i.e., $E_\perp(\kappa_\perp)$ and $E_\parallel(\kappa_\parallel)$ for $t = 0$, $10\tau_f$, $20\tau_f$, and $30\tau_f$. Figure 10(a) shows that energy levels increase progressively for $\kappa_\perp < \kappa_f$, whereas for $\kappa_\perp > \kappa_f$, the distribution of energy is nearly unaltered. Also for $\kappa_\perp > \kappa_f$, we observe that a narrow wave-number range develops from the initial state and approaches best a $\kappa_\perp^{-5/2}$ scaling law. Regarding $E_\parallel(\kappa_\parallel)$ [Fig. 10(b)], the energy content for $\kappa_\parallel > \kappa_f$ is significantly lower than at the onset of rotation. This corroborates the idea that rotation lessens the flow field dependency on the direction parallel to the rotation axis. As time evolves, the range $\kappa_\parallel < \kappa_f$ resembles best a $\kappa_\parallel^{-1/2}$ scaling law for all instants in time. We emphasize that this result is essentially different from predictions of the weak inertial-wave theory, as the latter estimates $E(\kappa_\parallel) \sim \kappa_\parallel^{-1/2}$ for $\kappa_\parallel$ larger than the forcing wave number.

IV. DISCUSSION

This work investigated through direct numerical simulations the effects of domain size and rotation rate on the energy cascade direction of rotating turbulence. The data presented here add substantially to previous work, which, in contrast, focused on smaller and shallower domains ($\kappa_f\mathcal{L}_\parallel$ and $\kappa_f\mathcal{L}_\perp < 8$ [19,22]). The presented results, therefore, contribute towards a complete picture of the phase diagram, which unveils the

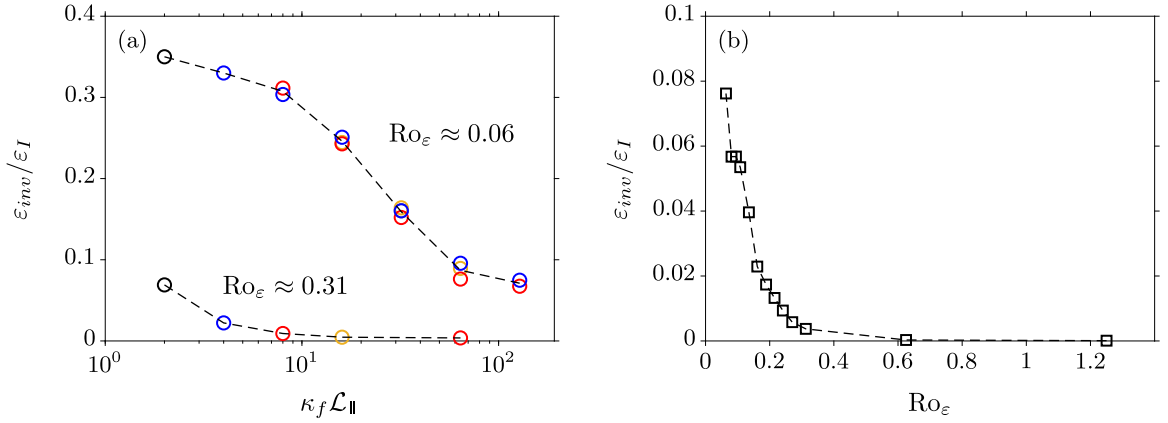

FIG. 5. Phase transition diagram for weak and strong rotation and varying geometrical dimensions (a) and for constant geometrical dimension and varying Ro_ε (b). Color scheme in (a) is the same as that in Fig. 3. In (a), the data point for $\kappa_f\mathcal{L}_\perp = \kappa_f\mathcal{L}_\parallel = 32$ (case `kf32-a01`) is almost identical to that for case `kf04-a08` ($\kappa_f\mathcal{L}_\perp = 4$; $\kappa_f\mathcal{L}_\parallel = 32$) and is therefore not visible.

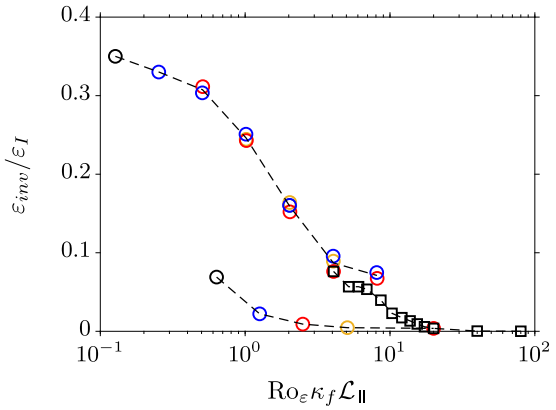

FIG. 6. Phase transition diagram in terms of the combined control parameter $\mathrm{Ro}_\varepsilon \kappa_f \mathcal{L}_\parallel$ for all data points in Fig. 5. Colored circles represent data from Fig. 5(a); squares, data from Fig. 5(b).

transition from inverse to forward through a split energy cascade in rotating turbulence.

Our results support $\kappa_f \mathcal{L}_\parallel$ as the primary control parameter provided that Ro_ε is constant and $\kappa_f \mathcal{L}_\perp > 4$. In this scenario, transversal finite-size effects of $\kappa_f \mathcal{L}_\perp$ on the inverse energy transfer $\varepsilon_{\mathrm{inv}}$ are negligible for our cases with aspect ratio $A_r \geqslant 1$. For weak rotation with $\mathrm{Ro}_\varepsilon \approx 0.31$, the transition from a split to a forward cascade was observed at $\kappa_f \mathcal{L}_\parallel \approx 64$.

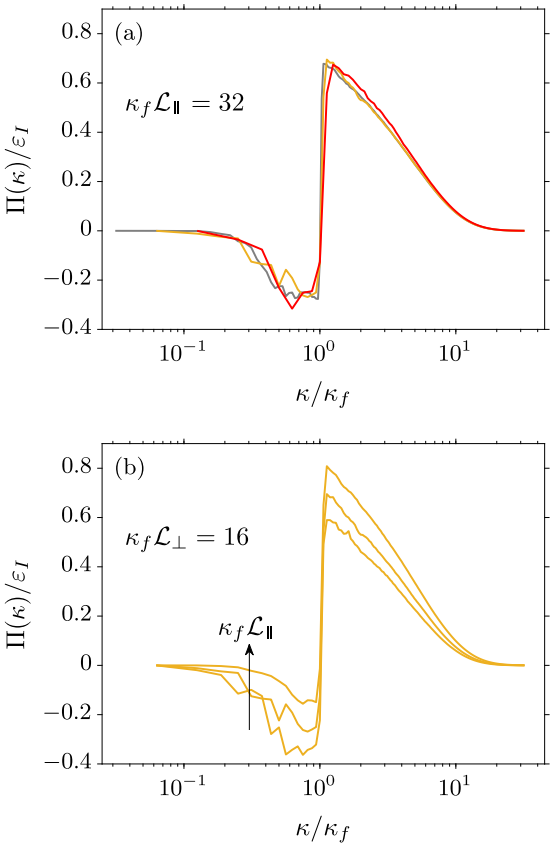

FIG. 7. Spectral energy flux for $\mathrm{Ro}_\varepsilon \approx 0.06$ and cases with $\kappa_f \mathcal{L}_\parallel = 32$ (a) and $\kappa_f \mathcal{L}_\perp = 16$ (b). In (a), $\kappa_f \mathcal{L}_\perp = 8$ (—), $\kappa_f \mathcal{L}_\perp = 16$ (—), and $\kappa_f \mathcal{L}_\perp = 32$ (—). In (b), $\kappa_f \mathcal{L}_\parallel = 16$, 32, and 64 (—). The arrow denotes the direction of increase.

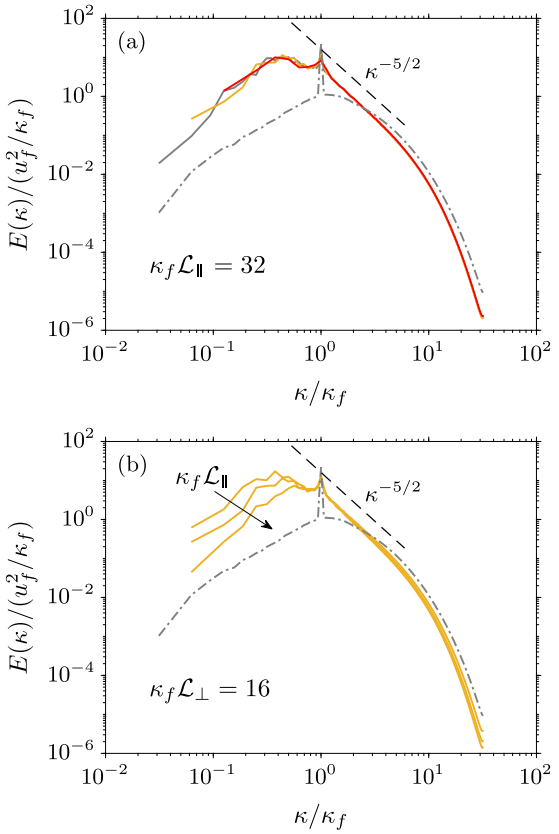

FIG. 8. Three-dimensional spherically averaged energy spectrum for $\kappa_f \mathcal{L}_\parallel = 32$ (a) and $\kappa_f \mathcal{L}_\perp = 16$ (b) with $\mathrm{Ro}_\varepsilon \approx 0.06$. Line styles are the same as in Fig. 7, apart from the reference energy spectrum in Fig. 1 with $\kappa_f \mathcal{L}_\perp = \kappa_f \mathcal{L}_\parallel = 32$ (— — —).

For the strong rotating case, however, although strongly suppressed, a portion of the injected energy ($\varepsilon_{\mathrm{inv}} \approx 0.075\, \varepsilon_I$) still cascaded inversely and accumulated at the large scales for $\kappa_f \mathcal{L}_\parallel = 128$.

We attribute the fact that $\varepsilon_{\mathrm{inv}}$ does not become exactly 0 for $\mathrm{Ro}_\varepsilon \approx 0.31$ to two effects. First, the simulations considered

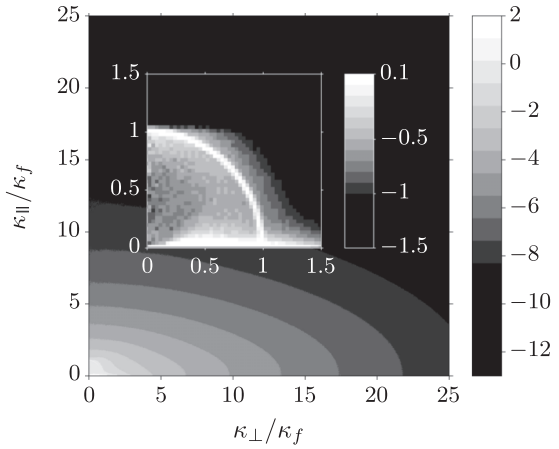

FIG. 9. Two-dimensional energy spectrum for $\mathrm{Ro}_\varepsilon \approx 0.06$ with $\kappa_f \mathcal{L}_\perp = \kappa_f \mathcal{L}_\parallel = 32$ (case `kf32-a01`) at $t = 30\,\tau_f$. Data are normalized by $(2\pi\kappa_\perp)\, u_f^2/\kappa_f^3$ and plotted as $\log_{10}$. Inset: Highlight of the region around the forcing wave number: $\kappa_\perp/\kappa_f < 1.5$ and $\kappa_\parallel/\kappa_f < 1.5$.

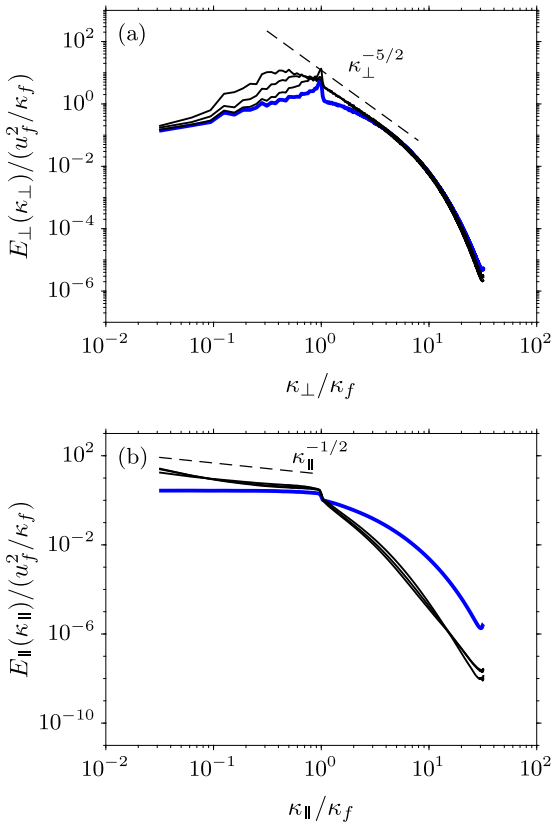

FIG. 10. One-dimensional energy spectra for $\mathrm{Ro}_\varepsilon \approx 0.06$ and $\kappa_f\mathcal{L}_\perp = \kappa_f\mathcal{L}_\parallel = 32$ (case `kf32-a01`) along directions $\kappa_\perp$ (a) and $\kappa_\parallel$ (b). Lines represent the time evolution of the energy spectrum: $t = 0$ (—), and $t = 10\tau_f$, $20\tau_f$ and $30\tau_f$ (—). A reference line for the scaling laws that best agrees with the presented data is also shown (- - -).

in this study are limited to $\mathrm{Re}_\lambda \approx 68$. A higher Reynolds number could contribute to a stronger forward cascade, possibly reducing $\varepsilon_{\mathrm{inv}}$ to 0. Second, although effects of the geometric nondimensional parameter $\kappa_f\mathcal{L}_\perp$ are minor, results hint that larger values of $\kappa_f\mathcal{L}_\perp$ could also contribute to a reduction of $\varepsilon_{\mathrm{inv}}$. In this manner, an indefinite increase in $\kappa_f\mathcal{L}_\perp$ could potentially change the phase diagram in the vicinity of $\varepsilon_{\mathrm{inv}}/\varepsilon_I = 0$, and could cause the regime transition to be sharp rather than smooth. The recent study by Benavides and Alexakis [21] has shown that a continuous increase in the horizontal domain dimensions shifts the transition behavior for thin-layer turbulence from smooth to critical. We hope that further studies will help to fill the parameter space for higher Reynolds numbers and even longer domain sizes.

For $\mathrm{Ro}_\varepsilon \approx 0.06$, we agree with Deusebio *et al.* [22] and believe that a continuous increase in $\kappa_f\mathcal{L}_\parallel$ would result in a transition to a forward energy cascade. Nevertheless, results for the weak case suggest a slow-paced transition and significantly larger values for $\kappa_f\mathcal{L}_\parallel$ might be required. Interestingly, the transition of $\varepsilon_{\mathrm{inv}}$ in terms of $\kappa_f\mathcal{L}_\parallel$ resembles a logistic function, similar to what has been found for regime transitions in thin-layer turbulence [21].

In the search for a criterion for transition between a forward and a split cascade system, we made an attempt to express $\varepsilon_{\mathrm{inv}}/\varepsilon_I$ for all parameter points as a function of $\mathrm{Ro}_\varepsilon\kappa_f\mathcal{L}_\parallel$. As the different curves do not overlap, we believe that a criterion for transition should stem from a more general match of time scales. A criterion such as $\mathrm{Ro}_\varepsilon\kappa_f\mathcal{L}_\parallel = C$ can be obtained by requiring the slowest inertial wave frequency $1/\tau_w = 2\Omega/\kappa_f\mathcal{L}_\parallel$ and the eddy turnover frequency $u_f\kappa_f$ at the forcing scale to be of the same order [2,23]. Alternatively, we can frame the problem within the idea that rotation alters the spectral transfer time τ_s at which energy is transferred to smaller scales. Thus, it follows that $\varepsilon_v \sim u_\ell^2/\tau_s$, with u_ℓ a velocity scale characteristic of eddies of size ℓ, and $\tau_s \sim \tau_{\mathrm{nl}}^2/\tau_3$ [17,30,31]. Here, $\tau_{\mathrm{nl}} \sim \ell/u_\ell$ is the nonlinear time scale and τ_3 is the relaxation time of triple velocity correlations. The relaxation time in isotropic turbulence simplifies to τ_{nl} to recover the dissipation law, i.e., $\varepsilon_v \sim u_\ell^3/\ell$.

Now the condition $\mathrm{Ro}_\varepsilon\kappa_f\mathcal{L}_\parallel = C$ can be obtained by requiring $\varepsilon_v = \varepsilon_I$ and assuming $u \sim u_f$, $\tau_{\mathrm{nl}} \sim \tau_f$, and $\tau_3 \sim \tau_w$. So, $\mathrm{Ro}_\varepsilon\kappa_f\mathcal{L}_\parallel = C$ is equivalent to stating that in the presence of rotation the nonlinear time scale remains of the order of τ_f and that the relaxation time scale τ_3 is given by the inverse of the slowest inertial-wave frequency, i.e., $\tau_3 \sim \tau_w$. A generalization of the previous reasoning would be to consider a τ_{nl} obtained from a measured velocity quantity, like the r.m.s velocity, and the length scale ℓ, possibly as $\ell_\perp$, as the triadic interactions are expected to be depleted in the direction parallel to the rotation axis [32]. The relaxation time τ_3 could be sought as a function of both τ_f and τ_Ω. In this manner, more general criteria like $\mathrm{Ro}_\varepsilon{}^a(\kappa_f\mathcal{L}_\parallel)^b = C$ arise, where a and b are yet undetermined exponents.

Results for scaling laws of the energy spectrum are here not conclusive, and there is no clear sign of an inertial range over several decades. This is plausible since our initial and isotropic field with $\mathrm{Re}_\lambda \approx 68$ does not contain a clear inertial range. In spite of that, the narrow wave-number region after $\kappa_\perp = \kappa_f$ develops and approaches best a $\kappa_\perp^{-5/2}$ scaling law. Our results also show that the $\kappa_\perp^{-5/2}$ and $\kappa_\parallel^{-1/2}$ scalings appear in different wave-number ranges, and that the $\kappa^{-5/2}$ scaling prevails in the 3D energy spectrum (see Fig. 8).

ACKNOWLEDGMENTS

The authors would like to thank Dr. Alexandros Alexakis for stimulating discussions and helpful advice. This work was carried out on the Dutch national e-infrastructure with the support of the SURF cooperative and the Netherlands Organisation for Scientific Research (NWO).

[1] U. Frisch, *Turbulence: The Legacy of A. N. Kolmogorov* (Cambridge University Press, Cambridge, UK, 1995).
[2] A. Alexakis and L. Biferale, Phys. Rep. **767–769**, 1 (2018).
[3] G. Boffetta and R. E. Ecke, Annu. Rev. Fluid Mech. **44**, 427 (2012).
[4] H. P. Greenspan, *The Theory of Rotating Fluids* (Cambridge University Press, Cambridge, UK, 1968).
[5] F. S. Godeferd, F. Ed, and E. Moisy, Appl. Mech. Rev. **67**, 030802 (2015).
[6] F. Waleffe, Phys. Fluids A **5**, 677 (1993).

[7] C. Cambon, N. N. Mansour, and F. S. Godeferd, J. Fluid Mech. **337**, 303 (1997).
[8] L. Smith and F. Waleffe, Phys. Fluids **11**, 1608 (1999).
[9] M. Buzzicotti, H. Aluie, L. Biferale, and M. Linkmann, Phys. Rev. Fluids **3**, 034802 (2018).
[10] P. K. Yeung and Y. Zhou, Phys. Fluids **10**, 2895 (1998).
[11] P. D. Mininni, A. Alexakis, and A. Pouquet, Phys. Fluids **21**, 015108 (2009).
[12] F. Moisy, C. Morize, M. Rabaud, and J. Sommeria, J. Fluid Mech. **666**, 5 (2011).
[13] P. D. Mininni, D. Rosenberg, and A. Pouquet, J. Fluid Mech. **699**, 263 (2012).
[14] A. Delache, C. Cambon, and F. Godeferd, Phys. Fluids **26**, 025104 (2014).
[15] M. Linkmann and V. Dallas, Phys. Rev. Fluids **2**, 1 (2017).
[16] H. K. Moffatt, J. Fluid Mech. **741**, R3 (2014).
[17] S. Galtier, Phys. Rev. E **68**, 015301 (2003).
[18] S. Nazarenko, *Wave Turbulence*, *Lecture Notes in Physics* (Springer, Berlin, 2011).
[19] L. M. Smith, J. R. Chasnov, and F. Waleffe, Phys. Rev. Lett. **77**, 2467 (1996).
[20] A. Celani, S. Musacchio, and D. Vincenzi, Phys. Rev. Lett. **104**, 184506 (2010).
[21] S. J. Benavides and A. Alexakis, J. Fluid Mech. **822**, 364 (2017).
[22] E. Deusebio, G. Boffetta, E. Lindborg, and S. Musacchio, Phys. Rev. E **90**, 023005 (2014).
[23] K. Seshasayanan and A. Alexakis, J. Fluid Mech. **841**, 434 (2018).
[24] S. A. Orszag, J. Fluid Mech. **49**, 75 (1971).
[25] D. Pekurovsky, SIAM J. Sci. Comput. **34**, C192 (2012).
[26] R. S. Rogallo, NASA Technical Memo **73**, 203 (1977).
[27] Y. Morinishi, K. Nakabayashi, and S. Q. Ren, Int. J. Heat Fluid Flow **22**, 30 (2001).
[28] K. Alvelius, Phys. Fluids **11**, 1880 (1999).
[29] V. Dallas, S. Fauve, and A. Alexakis, Phys. Rev. Lett. **115**, 204501 (2015).
[30] R. H. Kraichnan, Phys. Fluids **8**, 1385 (1965).
[31] Y. Zhou, Phys. Fluids **7**, 2092 (1995).
[32] S. V. Nazarenko and A. A. Schekochihin, J. Fluid Mech. **677**, 134 (2011).